Polarized light reflection from strained sinusoidal surfaces

Brian Schulkin, Hee C. Lim, Nejat Guzelsu, Glen Jannuzzi, and John F. Federici

We propose optical polarization imaging as a minimally invasive technique for measuring the mechanical properties of plastics and soft tissues through their change in reflectance properties with applied strain or force. We suggest that changes in surface roughness are responsible for the linear reflectivity changes with applied stretch or strain. Several aspects of this model are tested, including the dependence on the angle of incidence, the change in scattering and absorption coefficients with strain, and the lateral spatial resolution. The application of the technique to multilayer structures such as skin and competing optical effects such as laser speckle are discussed. © 2003 Optical Society of America

OCIS codes: 120.6660, 170.3660, 170.7050.

1. Introduction

Several groups have used the reflection of polarized light to image tissues such as skin.[1–6] In using polarized light, one can take advantage of that fact that linearly polarized light becomes increasingly randomly polarized as it propagates through the skin because of its large scattering coefficient. Linearly polarized light with cross-polarizing filters has been used in lens photography to investigate the skin surfaces and to improve anterior segment photography.[2–6] Light that is reflected from the skin has two components. The first one, which maintains the polarization of the incident light, is the regular reflectance that comes predominately from the surface of the skin. The second component comes from within the tissue and is due to backscattering of light from the various skin layers. The backscattered light is predominately randomly polarized because of the large scattering coefficient of the skin. Using a polarized light source and another polarizer in front of the camera parallel to the first polarizer (in front of the light source), researchers have observed skin surface details from the reflected light (surface reflection). In crossed-polarization they eliminate the surface reflection and preferentially detect the diffusely backscattered light. From the backscattering light reflection they obtain information about pigmentation, erythema, infiltrates, vessels, and other intracutaneous structures.

The polarization properties of reflected or transmitted light depend on the number of scattering events that take place for each photon.[1] For photons that suffer virtually no scattering events (so-called ballistic photons), their polarization properties are preserved. As photons participate in more and more scattering events, their final polarization state becomes more randomized. In the limit of many scattering events in a turbid tissue such as skin, the outgoing photons (diffusive photons) are unpolarized with equal-intensity components parallel and perpendicular to the polarization of the incident light. Although the diffusive photons can provide information along the tissue's thickness (depending on the penetration depth of the light source), it is difficult to determine which areas of tissue were sampled because of the multiple scattering events. On the contrary, ballistic photons are partially reflected whenever there is an index of refraction difference from one tissue layer into another. Hence the diffusive photons generally contribute to a background noise in every direction that masks the tissue imaging information carried by the ballistic photons. In the two-dimensional polarization imaging technique,[1] as well as other similar polarization measurements,[7,8] the perpendicular component of diffusely

B. Schulkin, H. C. Lim, G. Jannuzzi, and J. F. Federici (federici@njit.edu) are with the Department of Physics, New Jersey Institute of Technology, University Heights, Newark, New Jersey 07102. N. Guzelsu is with the Biomechanics Laboratory, School of Osteopathic Medicine, University of Medicine and Dentistry of New Jersey, Stratford, New Jersey 08084 and is also with the Bioengineering Program, Rutgers University, Trailer 4, 675 Hoes Lane, Piscataway, New Jersey 08854.

Received 25 February 2003; revised manuscript received 11 June 2003.

0003-6935/03/255198-11$15.00/0

© 2003 Optical Society of America

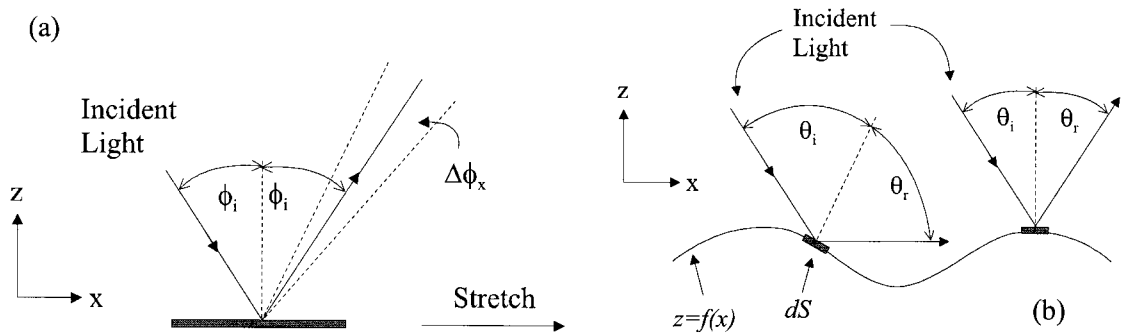

Fig. 1. (a) Geometry of the effective angle of incidence ϕ_i and the detection angle $\Delta\phi_x$. All light rays reflected from the surface within the detection angle contribute to the detected light in the specular reflection direction. The material is stretched parallel to the plane of incidence. (b) Geometry of the local angle of incidence θ_i for two different locations on the undulating surface topology. For regions of the surface for which the vector normal to the surface dS is oriented close to the $\hat{z}$ direction, the reflected light is within the detection angle $\Delta\phi_x$.

reflected light is subtracted from the parallel component (ballistic plus diffusive) to remove the background noise.

Recently we reported that polarization imaging can be used to measure some of the mechanical properties of stretchable materials such as plastic as well as soft tissues such as skin.[7,8] This optically based minimally invasive, noncontact, *in situ* technique that is used to measure strain is based on changes in the reflectivity of polarized light as the soft material is stretched. It has been suggested that, as the material is stretched, the surface roughness is reduced resulting in a smoother reflecting surface and a commensurate increase in the polarized reflected light. A simple model of surface roughness predicts[7] that the reflectivity should vary linearly with strain as is observed experimentally. In addition to the measurement of strain in diffusely reflecting plastics, polarization imaging might find use in minimally invasive measurements of tissue strain such as wound closure, healing, and scar tissue formation.[8] In this paper we test various aspects of the surface roughness model for polarization imaging measurements of plastics and investigate its lateral spatial resolution. In Section 2 we develop the theoretical model for light reflection from a rough surface. In Sections 3 and 4 we describe the details of our experimental measurements for testing various aspects of the model. In Section 5 we discuss applications of the technique to measurements of multilayered materials such as skin. We summarize our conclusions Section 6.

2. Theoretical Formulation

Our previous theoretical analysis of polarization imaging of stretchable materials assumed a simple two-dimensional model for the position of the boundary z between two surfaces (e.g., air and plastic or air and skin)[7]:

$$z = A \sin(gx) , \tag{1}$$

where A is the height of the surface boundary with a spatial scale of $s = 2\pi/g$. This periodic model was originally suggested for the surface roughness of the skin and is used to explain how the surface patterns of the skin change because of tension loads.[9]

The spatial scale of the surface undulations s can be related to the horizontal length of the sample $l = sM$ where M is the number of oscillations in the surface. (The length l is not the same as the length of the undulating surface profile L that is defined in Subsection 2.E.) From Eq. (1) the strain applied to the sample can be written as $\varepsilon = (l - l_0)/l_0 = (s - s_0)/s_0$ where l is the horizontal length of the sample after stretching and l_0 is the unstretched length.

The detected reflected power from the surface can be expressed as[7]

$$P(\phi_i) = -\iint I_0 \hat{k} \cdot \mathbf{dS} r(\theta_i) , \tag{2}$$

where I_0 is the incident intensity (power/area) of the illuminating light (assumed to be constant), $\hat{k}$ is a unit vector in the direction of the incident radiation, **dS** is an infinitesimal area element of the surface defined by $z = A \sin(gx)$, $r(\theta_i)$ is the local reflectivity coefficient for light interacting with the local surface at incident angle θ_i, and the double integral is evaluated over the portion of the surface that reflects light into an optical detector. The geometry of the local angle of incidence θ_i, the effective angle of incidence ϕ_i, and detection angle $\Delta\phi_x$ is shown in Fig. 1. Interference among the various rays of light reflecting from the surface (laser speckle) is ignored. In the theoretical treatment that follows, the diffusive component to the reflected power is neglected. This is justified because the polarization imaging measurement technique removes the contribution of the diffusive (unpolarized) component from the experimental data. Therefore the specularly reflected power will be dominated by light reflection from boundaries for which there is an index of refraction mismatch.

If the function $z = f(x, y)$ maps the surface of the

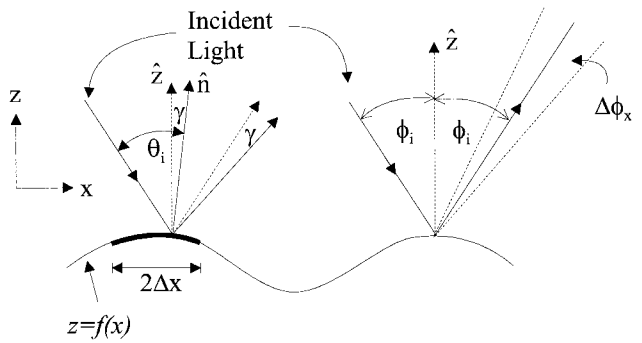

Fig. 2. Illustration of light reflection from a surface. The point on the right illustrates light reflected from a point of zero slope. At this point, the local angle of incidence is the same as the effective angle of incidence ϕ_i. Light reflected within an angle of $\Delta\phi_x$ of the specular reflection direction is detected. The point on the left illustrates the relation between the normal to the surface and the z direction.

material, then one can use the following identities from vector calculus[10]:

$$\mathbf{dS} = \frac{\nabla[z - f(x, y)]}{|\nabla[z - f(x, y)]|}\, dS\,, \tag{3}$$

$$\iint G(x, y, z)dS = \iint G[x, y, f(x, y)] \times |\nabla[z - f(x, y)]|\mathrm{dxdy}\,, \tag{4}$$

where G is a function of x, y, and z. In Eq. (4) an integral is converted over a three-dimensional surface to an integral over the x–y plane. Equation (2) then becomes

$$P(\phi_i) = -\iint I_0\, \hat{k} \cdot \nabla[z - f(x, y)]r(\theta_i)\mathrm{dxdy}\,. \tag{5}$$

From the geometry defined in Fig. 1, $\hat{k} = -\cos\phi_i\,\hat{z} + \sin\phi_i\,\hat{x}$. The double integral is evaluated over the ranges of x and y such that the surface reflects light into the detector.

A. Determination of Limits of Integration

Light is detected in the specular reflection direction within a small solid angle as shown in Fig. 1(a). This implies that the portions of the surface that will reflect light in the specular direction satisfy the equation $\nabla f(x, y) \approx 0$. For these regions, the normal to the surface is nearly parallel to the z direction and the slope of the surface is nearly zero. We first consider a sinisoidal topology $z = A\sin(gx)$ with the strain applied in the x direction parallel to the plane of incidence. As illustrated in Fig. 2, the portions of the surface that reflect light into a detector within a collection angle determined by $\Delta\phi_x$ will have normal vectors close to $\hat{z}$. From Fig. 2, the angle γ must be sufficently small such that $|\hat{n} \times \hat{z}| = \sin\gamma \leq \sin\Delta\phi_x$ where the unit normal vector to the surface is $\hat{n} = \nabla[z - f(x, y)]/|\nabla[z - f(x, y)]|$ and $\Delta\phi_x$ is assumed to be small. For $f(x, y) = A\sin(gx)$, this condition becomes

$$\frac{|Ag\cos(gx)|}{[1 + A^2g^2\cos^2(gx)]^{1/2}} \leq \sin\Delta\phi_x\,.$$

For detection of specularly reflected light, $\Delta\phi_x$ is a small angle so that the range of x that satifies the above equation is given by $gx = (\pi/2 + g\Delta x)$, $(3\pi/2 + g\Delta x)$, $(5\pi/2 + g\Delta x)$, . . . The range of x near each topological peak in the surface that contributes to the detected light can be related to the maximum detection angle: $Ag^2\,\Delta x = \Delta\phi_x$.

B. Specular Reflection Limit

Two further simplifications can be made to Eq. (5) that are justified in Subsection 2.C: (a) The Fresnel reflectivity coefficient can be treated as an effective constant $r(\phi_i)$ and brought out of the integral. (b) The contribution to the integral from the $\nabla f(x, y)$ term can be neglected. These approximations are valid in the limit of a small collection angle $\Delta\phi_x$. With these simplifications, the detected power that will change with strain is then

$$P(\phi_i) = I_0\cos\phi_i r(\phi_i)\iint \mathrm{dxdy}\,, \tag{6}$$

where the integral is over the x–y plane of the surface with the correct range of tilts to reflect light into the detector.

C. Change of Fresnel Reflection Coefficient with Strain

Ultimately, one is interested in the change in detected reflected optical light that is due to applied strain. Taking the derivative ($s_0\partial/\partial s = \partial/\partial\varepsilon$) of Eq. (5), we obtain

$$\frac{\mathrm{d}P(\phi_i)}{\mathrm{ds}} = -\iint\left(\frac{\partial\{I_0\hat{k}\cdot\nabla[z - f(x, y)]\}}{\partial s}\, r(\phi_i) + \{I_0\hat{k}\cdot\nabla[z - f(x, y)]\}\,\frac{\partial r(\theta_i)}{\partial s}\right)\mathrm{dxdy}\,, \tag{7}$$

The leading term of the first term on the right-hand side of Eq. (7) is a constant independent of s as was shown in Ref. 7 and is shown here in more detail. Below we show that the leading term of the second term on the right-hand side of Eq. (7) is a higher-order term and can be neglected in the limit of a small detection angle. Refering to Eq. (7) and Fig. 3, the partial derivative of the Fresnel coefficient with strain has two contributions: one for which the slope of the topology is positive and one for which the slope is negative:

$$\frac{\partial r(\theta_i)}{\partial s} = \frac{\partial r(\theta_i)}{\partial[\cos(\theta_i)]}\,\frac{\partial(\cos\theta_i)}{\partial s}\,,$$

$$\frac{\partial(\cos\theta_i)}{\partial s} = \frac{\partial(\cos\theta_i)_+}{\partial s} + \frac{\partial(\cos\theta_i)_-}{\partial s}\,. \tag{8}$$

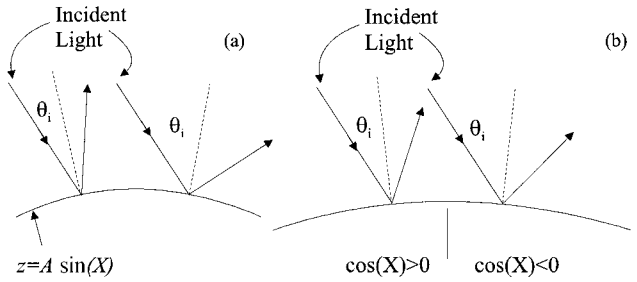

Fig. 3. Illustration of the change in local angle of incidence with stretch: (a) before stretch, (b) after stretch.

In regions of the topology for which the slope is positive, stretching increases the local angle of incidence, whereas regions for which the slope is negative tend to decrease the local angle of incidence with strain. The net result is that these two effects tend to cancel each other.

Calculating $\cos(\theta_i) = -\hat{k} \cdot \hat{n}$ yields

$$\cos(\theta_i) = \frac{\cos\phi_i + Ag\cos(gx)\sin\phi_i}{[1 + A^2g^2\cos^2(gx)]^{1/2}}$$

In taking the derivative with respect to strain of the above equation, we treat $X = gx$ as a contant. This is justified because one is interested in how the local angle of incidence changes near a topological peak where $\nabla f(x, y) = 0$. As the surface is stretched, the location of x where a peak occurs will change, but the phase $X = gx$ at which a peak occurs is invariant. In the limit of a small detection angle such that $\cos X \approx 0$, the leading term is

$$\frac{\partial[\cos(\theta_i)]}{\partial s} = \frac{\partial(Ag)}{\partial s}\cos(X)\sin\phi_i\,.$$

Because the above equation changes sign depending on whether one is to the left or right of the topological peak, $\partial[\cos(\theta_i)]_+/\partial s = -\partial[\cos(\theta_i)]_-/\partial s$ for symmetric positions about the peak. This implies that $\partial r(\theta_i)/\partial s = 0$ is approximately zero, and the second term of Eq. (7) is small compared with the first term and can be neglected. In this case, $r(\theta_i)$ can be approximated as $r(\theta_i)$ in Eqs. (5) and (7) and removed from the integrals.

In the same limit of a small detection angle, the $\nabla f(x, y)$ term vanishes in Eq. (5) because $\nabla f(x, y) \approx 0$ and the integral is symmetrically evaluated about this point of zero slope. Equation (5) becomes

$$\begin{aligned} P(\phi_i) &= -r(\phi_i)\iint I_0\hat{k}\cdot\nabla[z - f(x, y)]\mathrm{dxdy} \\ &= r(\phi_i)\iint I_0[\cos\phi_i - \sin\phi_i\hat{x}\cdot\nabla f(x, y)]\mathrm{dxdy}\,. \end{aligned} \tag{9}$$

The integration is evaluated only for a small range of x and y values near $\nabla f(x, y) \approx 0$. Assuming $\nabla f(x_0, y_0) = 0$, expanding the function as a Taylor series near this point yield. $f(x, y) = f(x_0, y_0) + \partial f/\partial x|_{x_0}(x - x_0) + \partial^2 f/\partial x^2|_{x_0}(x - x_0)^2/2 + \ldots$. The linear term in the expansion vanishes. The quadradic and constant terms are symmetric with respect to displacement from the point of zero slope. Consequently, when the antiderivative of $\hat{x}\cdot\nabla f\,\mathrm{dx}$ is evaluated about the symmetric points, the result is zero. Therefore the ∇f term of Eq. (9) is small compared with the first term in the limit of a small collection angle. The detected optical power that will change with strain is then approximately $P(\phi_i) = I_0\cos(\phi_i)r(\phi_i)\iint\mathrm{dx\,dy}$.

D. Dependance of Specularly Reflected Power on Strain

For $z = A\sin(gx)$, areas that contribute to Eq. (6) are given by solutions to $\cos(gx) \approx 0$. There are two zeros per cycle of the cosine. The integral in x of Eq. (6) can then be replaced by the integral over one of the narrow regions where the cosine is zero. Using $\Delta\phi_x = Ag^2\,\Delta x$ with $2N$ zeros and N equal to the number of illuminated oscillations, then $\int\mathrm{dx} = (2\Delta x)2N$ and the detected optical power become

$$P(\phi_i) = P_0 r(\phi_i)\,\frac{\Delta\phi_x}{L_x}\,\frac{4N}{Ag^2}\,, \tag{10}$$

where the integration over y yields L_y, the horizontal length in the y direction of the illuminated area, and $P_0 = I_0\cos\phi_i\,L_xL_y$ is the total incident power on the surface. The number of peaks illuminated can be written as $N = L_x/(2\pi/g)$, which is just the horizontal length of the area illuminated by the incoming light divided by the spatial scale length of the surface undulations. Note that with this definition the number of peaks illuminated will change with strain. This is correct because, as the surface is stretched, some peaks will no longer be within the illuminated area. Substituting this expression into the Eq. (10) yields

$$P(\phi_i) = P_0 r(\phi_i)\,\frac{\Delta\phi_x}{Ag}\,\frac{2}{\pi}\,. \tag{11}$$

To write Eq. (11) only in terms of the strain, one needs to relate the amplitude A and the spatial scale $s = 2\pi/g$ of the topology to the strain of the material. We now follow our previous analysis[7] and assume that the length of the surface remains constant as the material is stretched. In the x direction, the length of the surface is calculated from

$$\begin{aligned} L &= \int|\nabla[z - f(x, y)]|\mathrm{dx} \\ &= \int[1 + A^2g^2\cos^2(gx)]^{1/2}\,\mathrm{dx}\,, \end{aligned}$$

where the limits of integration are over the physical limit of the material in the x direction. Because the total number of oscillations of the surface M is constant, the above integral can be cast into the length of

the surface over a single cycle times the number of cycles. Substituting $gx = \partial$ yields

$$L = \frac{M}{g}\int_0^{2\pi} [1 + A^2g^2\cos^2(\vartheta)]^{1/2}\,\mathrm{d}\vartheta$$
$$= \frac{M}{g}(1 + A^2g^2)^{1/2}\,E(2\pi|\alpha)\,, \qquad (12)$$

where $E(2\pi|\alpha)$ is an elliptic integral of the second kind and $\alpha \equiv \sin^{-1}\{[A^2g^2/(1 + A^2g^2)]^{1/2}\}$.

In the limit of rough surfaces, $Ag \gg 1$, $\alpha = \pi/2$, and $E(2\pi \mid \pi/2) = 4$. This implies that $L = 4MA$ approximately. In this rough-surface limit, the amplitude of the surface ripple is approximately constant. The reflected power changes predominately because of changes in the periodicity of the surface ripples. In this limit, Eq. (11) becomes

$$P(\phi_i) = P_0 r(\phi_i)\Delta\phi_x \frac{4sM}{\pi^2 L}\,, \qquad (13)$$

where $s = 2\pi/g$ was substituted.

E. Numerical Solution and Verification of the Analytic Solution

To justify the approximations that are used to derive Eq. (13), Eq. (5) is numerically integrated with MATLAB. As with the analytic solution, it is assumed that a large number of topological peaks are illuminated. The Fresnel reflection coefficient and angle of incidence are a function of position along the sinusoidal surface. For the numerical evaluation, the surface is broken into a grid with a grid spacing of 10^{-4} of a sinusoidal oscillation. At each grid position, the reflected power and corresponding direction of the reflected light are calculated. Light that is within the solid angle of collection $\Delta\phi_x$ contributes to the total reflected power. Results of these numerical simulations are compared with the analytic solution to Eq. (13) as well as with experimental results. The relation between amplitude A and spatial frequency g as the material is strained is found when we solve Eq. (12) assuming that the surface length L remains constant during the stretch.

There is a linear relationship between the numerically calculated reflectance and the strain as shown in Fig. 4. Within the first 20% of strain, the data are roughly linear. Insight into the origin of the linear slope can be attained when Ag versus g is plotted for a given L in Eq. (12). Over a wide range $0.5 < Ag < 10$, Ag is roughly proportional to g as shown in the inset of Fig. 4. This implies from Eq. (11) that the specularly reflected light is proportional to length $l = Ms$ of the sample ($s = 2\pi/g \propto 1/Ag$) over a wide range of values for Ag.

3. Experimental Setup

To test the validity of the rough-surface model, two aspects of the model are investigated experimentally. The first aspect is the dependence of the reflectivity gradient (slope of reflectivity versus strain curve) on

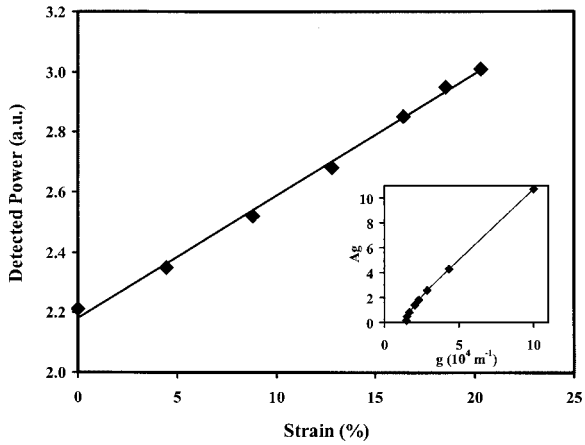

Fig. 4. For this numerical solution, $M = 400$, the illuminated spot size is 1 mm by 1 mm and $Ag \sim 2$. The specularly reflected power is calculated for 0° incidence with a solid angle of 0.0054 Sr. The numerical solution is well represented by a linear fit for the first 20% strain. The solid line is a linear fit to the data. The inset is a plot of Ag versus g for a fixed $L = 436$ μm in Eq. (12). Over a wide range, Ag is proportional to g suggesting that the $Ag \gg 1$ limit of Eq. (13) is valid over a wide range of Ag values.

the angle of incidence. From Eq. (13) the reflectivity gradient is

$$\frac{1}{P_0}\frac{\mathrm{d}P(\phi_i)}{\mathrm{d}\varepsilon} = \frac{s_0}{P_0}\frac{\mathrm{d}P(\phi_i)}{\mathrm{d}s} = r(\phi_i)\,\frac{\Delta\phi_x}{\pi^2 L}\,4l_0\,. \qquad (14)$$

Note that the reflectivity gradient depends on the Fresnel coefficient, the solid angle of collection, and the unstretched horizontal length l_0 and length of the surface L. By varying the angle of incidence for the incoming light, we determine if the measured reflectivity gradient is proportional to the Fresnel reflection coefficient as predicted by Eq. (14).

The second aspect to be tested is the dependence of the scattering (μ_s) and absorption (μ_a) coefficients as a function of strain. If the surface roughness changes as the soft tissue is stretched, there should be a corresponding reduction in the measured scattering coefficient. The effective attenuation coefficient can be derived from our analytical model discussed in Section 2. Consider the measurement of the collimated transmission through a material placed at normal incidence with respect to the incoming light. As the light interacts with the undulating front surface, the light is refracted at an angle determined by the local angle of incidence and the index difference between the air and the material. If the refraction angle were too large, the refracted light would not be within a small angle of detection for the collimated transmitted light. Consequently, with a single rough surface, the detected light is dominated by light rays that pass through the material near regions where the local slope $\nabla f(x, y) \approx 0$. The transmission geometry is analogous to Fig. 2 with the angle of incidence $\phi_i = 0$ and the range of Δx that contributes to the collimated transmission is determined by the local curvature of the topology. An

analogous manipulation of the equations of Section 2 can be performed with the same conclusion as the reflected light: The range of Δx that contributes to the collimated transmission varies as $\Delta x \sim \Delta\phi_t/Ag^2$, where $\Delta\phi_t$ is the detection angle of the transmitted light. The theoretical analysis of the transmitted light is essentially the same as the reflection analysis that led to Eq. (14): The change in the power of the collimated transmission is proportional to the change in strain of the material. From the collimated transmission, one can use a Beer–Lambert law to calculate the corresponding absorption and scattering coefficients:

$$P = P_0 \exp[-(\mu_a + \mu_s)d], \tag{15}$$

where μ_a and μ_s are the absorption and scattering coefficients of the material and d is the sample thickness.

A. Reflectivity Measurements

An experimental setup similar to our previous measurements is used[8] in which the angle of incidence can be varied from 0 to 80 deg. Linearly polarized light from a He–Ne laser ($\lambda = 632.8$ nm, $P < 5$ mW) is reflected from the sample. The reflected light is collected by a lens ($f = 50$ mm) after it passes through a polarizer (analyzer). The polarization of the incident light and the analyzer can be set in one of two perpendicular orientations: either parallel or perpendicular to the plane of incidence. The incident polarization is adjusted with a rotating half-wave plate to ensure equal intensities in either plane of polarization. We detect the laser power using the silicon photodetector by mechanically chopping the incident laser light and utilizing a lock-in amplifier and standard phase-sensitive detection techniques. The reflected power in both the parallel and the perpendicular polarization is measured as a function of the incident light polarization and sample strain. A simple device was built to apply stretch to the samples as described elsewhere.[8] Samples are stretched by equal displacement with the two computer-controlled translation stages. This allows the center of the sample to be stationary with respect to the stretch device. During the measurements, laser light is reflected from this central portion of the sample. Computer-controlled stepper motors are used to change the stretch of the sample in 100-μm steps. The stepper motors have a resolution of ± 1 μm. As is done with the polarization imaging method,[1,7,8] the component of the reflected light that is polarized perpendicular to the direction of the incident light is subtracted from the magnitude of the detected reflected light polarized parallel to the incident light. The samples used in the experiment are latex sheets. The front surfaces of the sheets are diffusely reflecting.

B. Integrating Sphere Measurements

If the change in specular reflection were due to changes in surface roughness as proposed, there should be a corresponding change in the scattering properties of the material with strain. To measure the sample's scattering and absorption coefficients, an integrating sphere arrangement is used as shown in Fig. 5. Using the integrating sphere technique in combination with an inverse adding–doubling algorithm,[11] we can determine the scattering (μ_s) and absorption (μ_a) coefficients as a function of strain. Linearly polarized light from a He–Ne laser ($P = 0.5$ mW) is directed on to the surface of the sample. The transmitted and reflected light is detected with 6-in. (15-cm) integrating spheres. Three detectors are used: one on each sphere and one to measure the incident light power. The sample is stretched from both ends by use of linear translation stages.

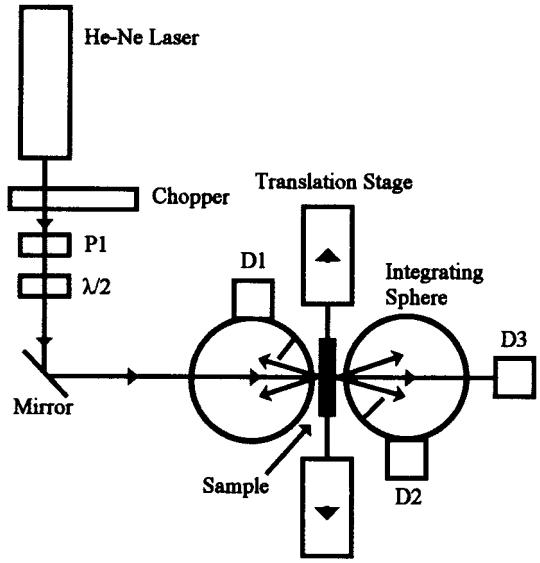

Fig. 5. Diagram of the integrating sphere measurement to determine the scattering and absorption coefficients of a sample as a function of strain.

4. Experimental Results

A. Angle of Incidence Results

To verify the angle of incidence dependence of the reflectivity gradient in Eq. (14), reflectivity measurements are performed for light polarized either parallel or perpendicular to the plane of incidence. The measured reflectivity gradients and those numerically calculated from Eq. (5) are shown in Fig. 6. The strain ε is defined as $\varepsilon = (\ell - \ell_0)/\ell_0$ where ℓ_0 and ℓ represent the length of the sample between the grips of the stretching device before and after the deformation, respectively. The solid curves are theoretical Fresnel reflection coefficients $r(\phi_i)$ for parallel and perpendicular polarizations of incident light. The similarity of the experimental data and numerical solutions to the theoretical Fresnel curves confirms the angle of incidence dependence in Eq. (14).

B. Diffused Reflectance

The diffuse reflectivity is measured with the integrating sphere arrangement of Fig. 5. The entrance

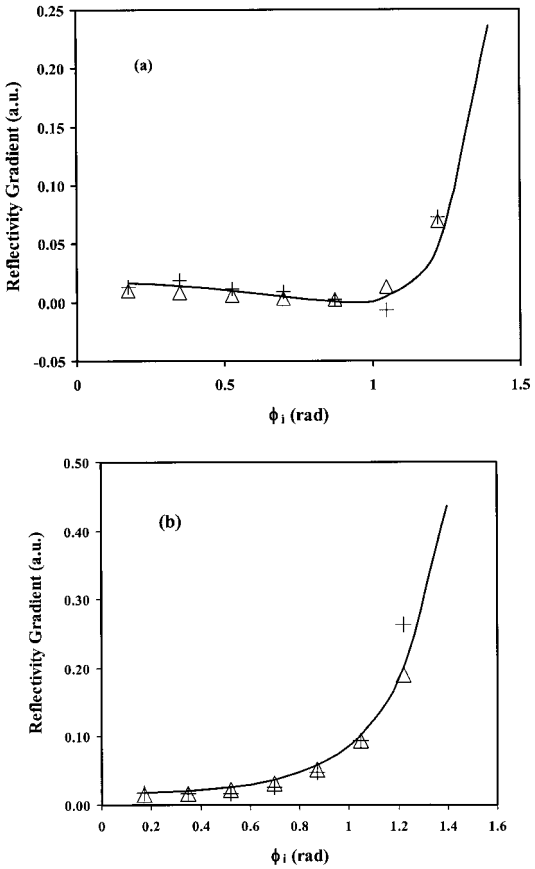

Fig. 6. Reflectivity gradient as a function of incident angle for (a) parallel and (b) perpendicular polarization. The crosses and triangles represent experimental measurements and numerical solutions to Eq. (5), respectively. The solid curves are the Fresnel reflection coefficient multiplied by a scaling factor. The parameters for the numerical simulation are $M = 400$, a detection angle of 0.0054 sr, and $Ag \sim 2$.

opening of the integrating sphere allows for specularly reflected light withing a solid angle of $\sim 6 \times 10^{-3}$ Sr to escape from the sphere. The diffuse reflectivity as a function of stain is shown in Fig. 7. The data show that, as the sample is stretched, the diffuse component of the reflectivity decreases by a small amount. Within the surface roughness model, this is expected because a decrease in surface roughness should lead to a smaller component of scattered light and an increase in the specularly reflected light. This experimental result is consistent with surface roughness measurements on *in vivo* human skin[9] that show that the surface roughness of skin is reduced by strain.

C. Optical Coefficients μ_a and μ_s

The absorption and scattering coefficients are determined from the integrating sphere measurements by the inverse adding–doubling method. The experimentally derived scattering ($\mu_s\, d$) and absorption ($\mu_a\, d$) are plotted in Figs. 8 and 9, respectively, as a function of strain. The effective thickness of the material is d. Both the absorption and the scattering

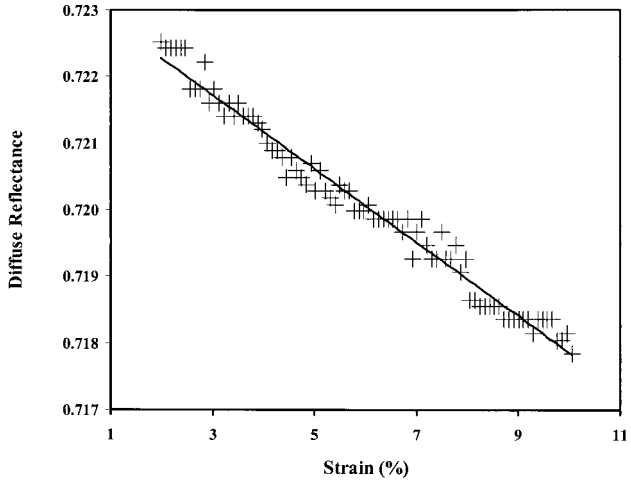

Fig. 7. Measured diffuse reflectance obtained with the integrating sphere technique. The solid line is a linear regression fit to the data. The unstretched length is 52.8 mm.

are linear functions of the strain. However, the optical properties are dominated by changes in the scattering with strain because the change in absorption coefficient is much less than the change in scattering. The decrease in the scattering with strain is consistent with a decrease in the surface roughness.

To compare the experimental results of Fig. 8 with our theory, the equivalent of Eq. (5) is numerically integrated for transmission geometry. Figure 10 shows the theoretical plot from our model of the transmitted power and total attenuation coefficient [$-\ln(P/P_0)$ from Eq. (15)] for collimated transmission. Note that, over the range of small strains (<20%), both lines are approximately linear. The collimated power scales linearly with strain as predicted by the theory presented in Sections 2 and 3. Moreover, the theoretically and experimentally measured attenuation coefficient both scale linearly with strain. However, there is an apparent discrepancy between the nearly linear dependence of both the

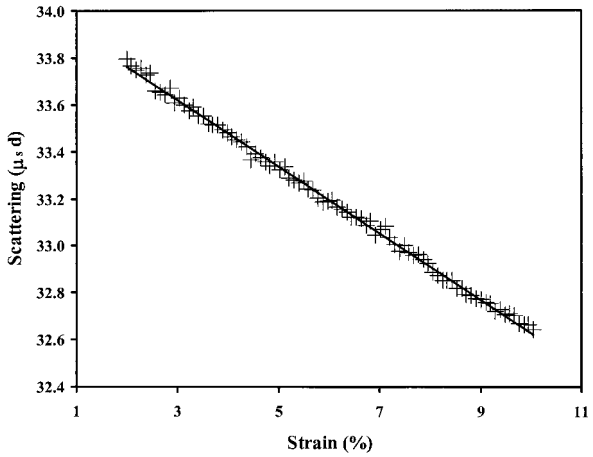

Fig. 8. Plot of experimentally measured scattering versus strain. The solid line is a linear fit to the data.

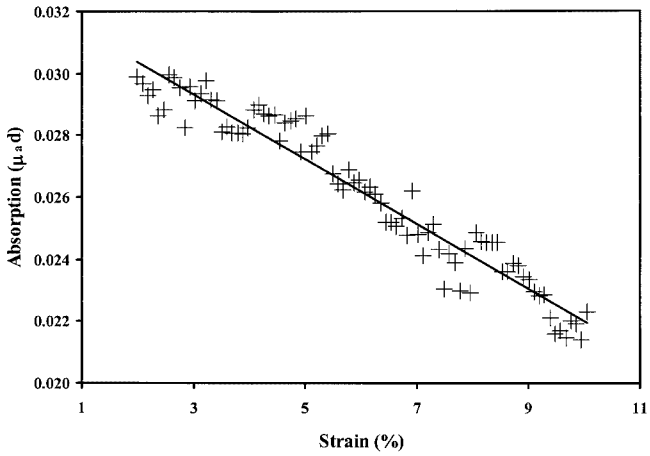

Fig. 9. Plot of experimentally measured absorption versus strain. The solid line is a linear fit to the data.

collimated power and the scattering coefficient as a function of strain. A simple Beer–Lambert law dependence [Eq. (15)] predicts that, if the scattering coefficient depends linearly on strain, then the detected power scales exponentially. This functional discrepancy can be explained by the fact that the change in the scattering coefficient with strain is small. In this limit, the exponential dependence of the power in Eq. (15) is approximately linear with strain.

D. Spatial Resolution and Laser Speckle

We investigated the lateral spatial resolution of the polarization imaging technique by illuminating an extended area of the sample with a He–Ne laser and

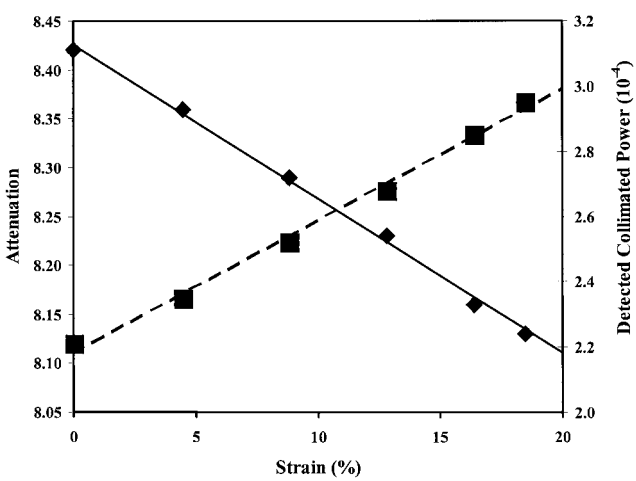

Fig. 10. For the same properties as Fig. 6, the calculated attenuation [from an equation similar to Eq. (5)] that is due to scattering (diamonds) decreases with strain, whereas the collimated transmitted power (squares) increases with strain. The solid lines are linear fits. If the scattering coefficient is written as a linear function of strain $\mu_s = \mu_0 (1 + \mu_{s1} \varepsilon/\mu_0)$, the best-fit parameters to the detected collimated power show that $\mu_{s1}/\mu_{s0} \ll 1$. In this case, $\exp(-\mu_s d)$ is approximately linear for small values of strain (<20%).

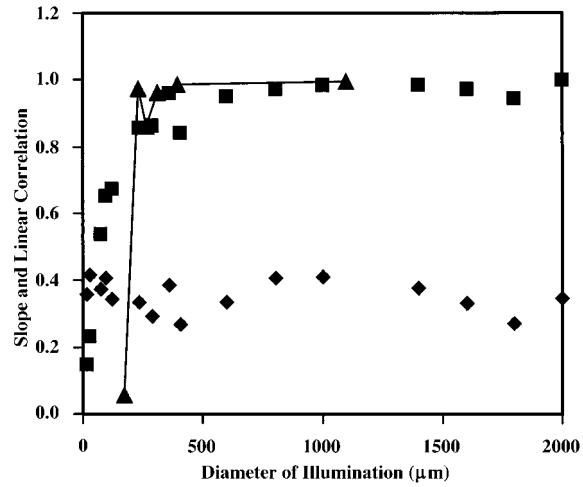

Fig. 11. Slope (diamonds) and linear correlation coefficient (squares) for data acquired with a CCD. The corresponding linear correlation coefficient obtained when the spot size of the laser beam was varied (triangle) is consistent with results obtained with the CCD. The significant drop in the correlation coefficient for the ~200-μm spot size suggests that this value is approximately the lateral spatial resolution needed to measure the strain of soft material with a coherent He–Ne laser source.

imaging the reflected light with a CCD camera (640 by 480 pixel Si array detector). Several images per strain position are acquired and then transferred to a computer to be analyzed. The digital image processing algorithms were written and computed with MATHCAD 7.0. By taking several frames of the same strain condition, we could average the images of several frames together to minimize random noise fluctuations of the imaged laser power that are due to laser speckle. The captured image is manipulated by an algorithm that is commonly utilized to analyze images with laser speckle; the total detected laser power within a specified area is calculated when the pixel count for all pixels within the specified area are summed and divided by the total number of summed pixels.[12] In applying this technique to our data to estimate the spatial resolution, we calculated the detected power as a function of strain from the CCD images by averaging the pixel counts within a certain radius of the center of the beam profile. Various diameters are used corresponding from 3 pixels across to 350 pixels across an equivalent 2-mm illuminated spot size. We calibrated the corresponding spatial resolution by measuring the width in pixels of the illuminated spot size on the sample (2 mm in diameter for 99% power).

The slope of the summed reflected power versus the strain curve is determined by linear regression. Typical results are plotted in Fig. 11 for the He–Ne laser source. As the radius of the summed area increases, the quality of the linear fit improves because of the averaging of a large number of pixels. As the pixel averaging area decreases, the linear correlation coefficient gradually decreases and then sharply

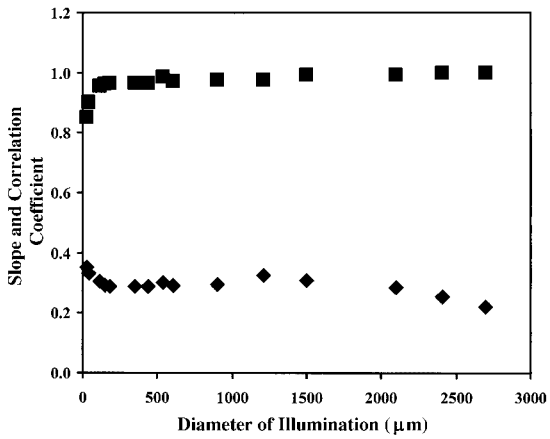

Fig. 12. LED source showing the results of reflectivity slope and linear correlation coefficient versus spot size by use of CCD detection.

drops for a spot size of roughly 200 μm. This spot size is consistent with experimental measurements when the single-element photodetector is used and the spot size of the laser beam is varied on the sample with a focusing lens.

To estimate the effect of laser speckle on the lateral spatial resolution, we replaced the He–Ne laser with an incoherent red LED. The data for the LED source are depicted in Fig. 12. The drop in the linear correlation coefficient near a spot size of 24 μm suggests that the lateral spatial resolution of polarization imaging on flexible plastic with the LED source is comparable to this value.

Within the proposed model of interface roughness for polarization imaging, it is assumed that the reflected light rays do not interfere with each other. This is strictly true if the illuminating light source is incoherent. For a coherent light source, interference between the various light rays scattering from the different surface bumps leads to the well-known speckle effect.[13] For large (~1-mm) laser spot sizes, interference among the various rays of light reflecting from the surface can be ignored. This approximation is valid because of the large area of illuminated tissue. For large spot sizes, the detected light contains many uncorrelated speckles arising from different locations on the sample surface. When all the collected light is detected by a single-element photodiode, any spatial fluctuations in light intensity that are due to laser speckle are averaged out.

5. Application to Multilayer Materials: Skin

When polarization imaging is applied to strain measurements of multilayer materials such as skin, the assumptions made in a single spatial-frequency, single-layer model and subsequent derivations are an oversimplification of the problem. However, in this section we show that Eqs. (6), (10), and (13) are essentially correct even when applied to multilayer structures such as skin. In applying our model to skin, we consider two complications: (a) the roughness of skin cannot be exactly represented by a single spatial frequency and (b) skin has a multilayered structure whereas the model presented concerns only a single-surface reflection.

Topological measurements of skin[9,14,15] show a rough surface that can be characterized by a characteristic height and spatial scale of the roughness (essentially the parameters A and g of our model). Ferguson and Barbenel[9] showed that, as human forearm skin is strained, the average height of the roughness decreases. When we use the measured roughness height ($A \sim 60$ μm) and spatial separation between major peaks ($2\pi/g = 350$ μm) from Ref. 9, Ag for the skin surface is approximately 1.1. Micrographs of the epidermis[16] suggest that the parameter $Ag \approx 6$ for the undulating base of the epidermis. This region is the germination layer for new cell growth. *In vitro* studies of skin strain have shown that the undulations (i.e., surface roughness) of the epidermal surface and dermoepidermal interface are flattened with strain before elongation of the cells occur.[17] Essentially, as the sublayers of skin are strained, the primary effect is that the roughness of the various skin layers decreases.

A. Nonsinusoidal Topology

The model can account for light reflection from a nonsinusoidal surface when we replace Eq. (1) with a generalized Fourier series:

$$f(x) = \sum_i A_i \sin(g_i x) + \sum_i B_i \cos(g_i x)\,, \qquad (16)$$

for which the integral of Eq. (6) is evaluated over the area of the surface that reflects light into the acceptance angle of the detector. As discussed in Section 2, it is assumed that the detection angle is small so that regions at which the slope of the topology vanishes, $\nabla f \approx 0$, contribute to the integral. Recall that in Section 2, Eq. (6) is valid in the limit of a small detection angle $\Delta\phi_x$. For a nonsinusoidal surface, the same conclusion holds if one considers each peak in the topology. The main difference is that the size of Δx in Fig. 2 depends on the local curvature of the topology near each peak. In this case, the size of the surface that contributes to the specularly detected reflected light is

$$\int \mathrm{dx} = \sum_j \Delta x_j\,,$$

where the sum is over the number of illuminated peaks. From this equation, we can define an effective Δx as

$$\int \mathrm{dx} = \sum_j \Delta x_j = \Delta x_{\mathrm{eff}} \sum_j w_j\,,$$

where w_j are the weighting factors for each illuminated peak. In determining the limits of integration of Eq. (6), we use as before $|\hat{n} \times \hat{z}| \leq \sin \Delta\phi_x$ where the

unit normal vector to the surface is $\hat{n} = \nabla|[z - f(x)]/|\nabla[z - f(x)]|$ and $f(x)$ is given by Eq. (16):

$$\frac{|\hat{z} \times \nabla f|}{(1 + |\nabla f|^2)^{1/2}} \leq \sin \Delta\phi_x .$$

For the jth peak in the topology located as x_j, $f(x)$ can be expanded as a Talyor-series expansion:

$$f(x) \approx f(x_j) + \frac{1}{2} \frac{\partial^2 f(x_j)}{\partial x^2} (x - x_j)^2 .$$

The linear term vanishes because the local slope vanishes at the peak. In this case, the limits of x integration for the jth peak can be determined from

$$\left| \frac{\partial^2 f(x_j)}{\partial x^2}(x - x_j) \right| = \left| \sum_i (A g_i^2 \sin g_i x_j + B_i g_i^2 \cos g_i x_j) \times (x - x_j) \right| \leq \Delta\phi_x . \quad (17)$$

In examining Eq. (17) we note that the range of $\Delta x = x - x_j$ that contributes to the specularly reflected light depends on the local curvature near each peak. Introducing an effective Δx defines the effective amplitude and spatial scale of the roughness:

$$\left| \sum_i (A g_i^2 \sin g_i x_j + B_i g_i^2 \cos g_i x_j)(x - x_j) \right| = \Delta x_{\text{eff}} A_{\text{eff}} g_{\text{eff}}^2 \leq \Delta\phi_x .$$

Evaluating Eq. (6) for a nonsinusoidal surface given by Eq. (17) yields Eqs. (10) and (13), provided that N, Ag^2, and L are interpreted as effective or average values for the rough surface. Therefore the linear increase of specular reflectivity with strain is a general property of rough surfaces and does not depend on the presence of a single sinusoidal spatial frequency.

B. Effect of Multiple Layers

In considering polarization imaging of a multilayered structure, one must assume that the absorption and scattering coefficients and indices of refraction are different for each layer. Because the detection angle $\Delta\phi_x$ is small when only specularly reflected light is detected, only ballistic photons will contribute to the measured reflectivity. Any scattered photons will be removed by the polarization imaging method (e.g., subtracting the orthogonal polarization removes the contribution from diffusive photons). Therefore the specularly reflected light contribution is dominated by the reflection of ballistic photons from the interfaces between the layers (i.e., whereever there is an index mismatch from one layer to the next). This implies that the laws of reflection and refraction at each interface dominate the specularly reflected light. The contribution to the detected power from each interface is weighted by the corresponding loss of ballistic photons in each layer, as determined by μ_s and μ_a. The roughness parameters A and g can then be interpreted as weighted averages that are averaged over the optical penetration depth of the light and roughness of the layers within that penetration depth.

6. Conclusion

The surface roughness model for polarization imaging of stretchable soft materials is investigated both experimentally and theoretically. The dependence of the reflectivity gradient with incident angle is measured and agrees with the functional dependence predicted by the surface roughness model. Integrating sphere measurements show that the integrated diffuse reflectivity decreases as a function of strain whereas the specularly reflected light increases. The optical properties of the material are dominated by scattering. As the material is strained, a smoother surface is produced that leads to a linear reduction in the measured scattering coefficient with strain. Because of relatively small changes in the scattering coefficient with strain, the corresponding change in the specularly reflected or transmitted optical power is also approximately linear with strain. The linear dependence of specular reflection is also expected for nonsinusoidal, multilayered structures.

References

1. S. G. Demos and R. R. Alfano, "Optical polarization imaging," Appl. Opt. **36,** 150–155 (1997).
2. R. R. Anderson, "Polarized light examination and photography of the skin," Arch. Dermatol. **127,** 1000–1005 (1991).
3. E. Fariza, T. O'Day, A. E. Jalkh, and A. Medina, "Use of cross-polarized light in anterior segment photography," Arch. Ophthalmol. (Chicago) **107,** 608–610 (1989).
4. J. Philp, N. J. Carter, and C. P. Lenn, "Improved optical discrimination of skin with polarized light," J. Soc. Cosmet. Chem. **39,** 121–132 (1988).
5. S. L. Jacques, J. R. Roman, and K. Lee, "Imaging superficial tissues with polarized light," Lasers Surg. Med. **26,** 119–129 (2000).
6. M. B. Ostermeyer, D. V. Stephensen, L. Wang, and S. L. Jacques, "Nearfield polariztion effects on light propagation in random media," in *Biomedical Optical Spectroscopy and Diagnostics*, E. Serick-Muraca and D. Benaron, eds., Vol. 3 of USA Trends in Optics and Photonics (Optical Society of America, Washington D. C., 1996), pp. 20–25.
7. J. F. Federici, N. Guzelsu, H. C. Lim, G. Jannuzzi, T. Findley, H. R. Chaudhry, and A. B. Ritter, "Noninvasive light reflection technique for measuring soft-tissue stretch," Appl. Opt. **38,** 6653–6660 (1999).
8. N. Guzelsu, J. F. Federici, H. C. Lim, H. R. Chauhdry, A. B. Ritter, and T. Findley, "Measurement of skin stretch via light reflection," J. Biomed. Opt. **8,** 80–86 (2003).
9. J. Ferguson and J. C. Barbenel, "Skin surface patterns and the directional mechanical properties of the dermis," in *Bioengineering and the Skin*, R. Marks and P. A. Payne, eds. MTP Press, Lancaster, UK, (1981), pp. 88–92.
10. E. W. Swokowski, *Calculus with Analytic Geometry*, 2nd ed. (Prindle, Weber and Schmidt, Boston, Mass., 1979).
11. S. A. Prahl, M. J. C. van Gemert, and A. J. Welch. "Determining the optical properties of turbid media by using the adding–doubling method," Appl. Opt. **32,** 559–568 (1993).
12. A. Weeks, Jr., Fundamentals of Electronic Image Processing (IEEE, New York, 1996), Chaps. 3 and 6.
13. T. Asakura, *Speckle Metrology* (Academic, New York, 1978), Chap. 8.
14. M. Assoul, M. Zahidi, P. Corcuff, and J. Mignot, "Three-

dimensional measurements of skin surface topography by triangulation with a new laser profilometer," J. Med. Eng. Technol. **18,** 11–21 (1994).
15. S. Makki, J. C. Barbenel, and P. Agache, "A quantitative method for the assessment of the microtopography of human skin," Acta Derm. Venereol. **59,** 285–291 (1979).
16. H. Gray, L. H. Bannister, M. M. Berry, and P. L. Williams, eds., *Gray's Anatomy* (Churchill Livingstone, London, 1995), pp. 376–381.
17. I. A. Brown, "A scanning electron microscope study of the effects of uniaxial tension on human skin," Br. J. Dermatol. **89,** 383–390 (1973).